The Equatorial Current System West of the Galápagos Islands during the 2014–16 El Niño as Observed by Underwater Gliders

DANIEL L. RUDNICK,[a] W. BRECHNER OWENS,[b] T. M. SHAUN JOHNSTON,[a] KRISTOPHER B. KARNAUSKAS,[c] JULIE JAKOBOSKI,[b] AND ROBERT E. TODD[b]

[a] *Scripps Institution of Oceanography, La Jolla, California*
[b] *Woods Hole Oceanographic Institution, Woods Hole, Massachusetts*
[c] *University of Colorado Boulder, Boulder, Colorado*

ABSTRACT: The strong El Niño of 2014–16 was observed west of the Galápagos Islands through sustained deployment of underwater gliders. Three years of observations began in October 2013 and ended in October 2016, with observations at longitudes 93° and 95°W between latitudes 2°N and 2°S. In total, there were over 3000 glider-days of data, covering over 50 000 km with over 12 000 profiles. Coverage was superior closer to the Galápagos on 93°W, where gliders were equipped with sensors to measure velocity as well as temperature, salinity, and pressure. The repeated glider transects are analyzed to produce highly resolved mean sections and maps of observed variables as functions of time, latitude, and depth. The mean sections reveal the structure of the Equatorial Undercurrent (EUC), the South Equatorial Current, and the equatorial front. The mean fields are used to calculate potential vorticity Q and Richardson number Ri. Gradients in the mean are strong enough to make the sign of Q opposite to that of planetary vorticity and to have Ri near unity, suggestive of mixing. Temporal variability is dominated by the 2014–16 El Niño, with the arrival of depressed isopycnals documented in 2014 and 2015. Increases in eastward velocity advect anomalously salty water and are uncorrelated with warm temperatures and deep isopycnals. Thus, vertical advection is important to changes in heat, and horizontal advection is relevant to changes in salt. Implications of this work include possibilities for future research, model assessment and improvement, and sustained observations across the equatorial Pacific.

KEYWORDS: Ocean; Tropics; Currents; El Nino; In situ oceanic observations

1. Introduction

The equatorial current system (ECS) in the eastern equatorial Pacific is an important element in global climate variability. Ocean–atmosphere interactions are central to the establishment of El Niños, including the ocean's crucial role in the zonal transport of mass, heat, and salt. Sustained ocean observations in the ECS include the Tropical Atmosphere Ocean (TAO) moored array (McPhaden et al. 2010) and the Argo array of profiling floats (Gasparin and Roemmich 2017; Riser et al. 2016), providing excellent resolution in depth and time across the equatorial Pacific. Reviews of the current state of sustained observations and plans for the future are in the Tropical Pacific Observing System plans (Smith et al. 2019). Less well observed is the meridional structure of such features as the Equatorial Undercurrent (EUC), the South Equatorial Current (SEC), and the equatorial front. The central observational goal of the Repeat Observations by Gliders in the Equatorial Region (ROGER) project was to quantify these features with fine horizontal resolution using underwater gliders (Rudnick et al. 2004; Rudnick 2016).

A standard reference for an observational description of the EUC is the seminal work of Johnson et al. (2002). That study used acoustic Doppler current profiler (ADCP) and conductivity–temperature–depth (CTD) data from ships, mostly those servicing the TAO array. The 172 meridional sections of velocity spanned the equatorial Pacific at ten different longitudes during the years 1985–2000, so that there were as many as 34 sections at a single longitude during that time period. The latitudinal separation between CTD stations was usually 1°, while the continuous profiling of the ADCP provided finer resolution. Results addressed the mean fields, the annual cycle and different phases of the El Niño–Southern Oscillation (ENSO) cycle. This work complements Johnson et al. (2002) with an intensive description of the EUC at the eastern terminus (and beyond) of the TAO array derived from several tens of sections over a few years spanning a strong El Niño.

A basic description of the oceanography of a region often involves the consideration of volume, heat, and salt variability. In the region west of the Galápagos where ROGER was located, the EUC dominates the circulation (Lukas 1986; Karnauskas et al. 2010). In this region, the eastward flowing EUC must slow at the equator as it is blocked by the islands, and also must be diverted meridionally to pass around the islands. The details of this diversion, and the rates of upwelling or downwelling that may also be involved, were recently addressed using data from ROGER (Jakoboski et al. 2020). Upper-ocean heat changes, especially during an El Niño event, are largely caused by heaving of the thermocline (Wyrtki 1975). The change in sign of planetary vorticity across the equator makes the region an excellent waveguide, with eastward propagating Kelvin waves a direct cause of this heaving. Evidence from the TAO moorings suggests that the EUC is modulated by these Kelvin waves (Roundy and Kiladis 2006). The EUC transports salty water from the western equatorial
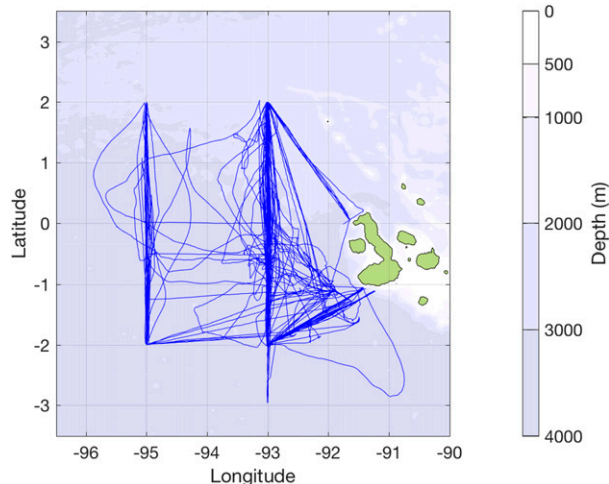
FIG. 1. Spray underwater glider tracks during ROGER, October 2013–October 2016.

FIG. 2. Sampling by Spray underwater gliders during ROGER along 93° (blue) and 95°W (red). Latitude and time are shown for each profile within 60 km of the respective longitudes.

Pacific, with the highest salinity in the southern part of the EUC (Johnson and McPhaden 1999; Johnson et al. 2002). The strong shear at the boundaries of the EUC leads to first-order effects by mixing (Moum et al. 2009; Warner and Moum 2019). The concurrent, high-resolution observations presented here address some of the mechanisms involved in balances of volume, heat, and salt.

ROGER was undertaken as a relatively short duration experiment, without special regard to the phase of the ENSO cycle. Deployments of Spray underwater gliders began in October 2013 and extended through October 2016. An El Niño serendipitously occurred during 2014–16, offering a special opportunity to observe the ECS in detail during the establishment and decay of the event. In this paper, we present observations of velocity, temperature, salinity, and such derived quantities as potential vorticity and Richardson number. Methods are presented in section 2, including the specifics of the glider sampling and the approaches used to calculate mean fields and objective maps. In section 3, the mean fields are considered as functions of latitude and depth. Variability is examined through maps as functions of time and latitude, and of time and depth. Time series indices of temperature, salinity, eastward velocity, and pycnocline depth help to understand the processes affecting heat and salt. Statistical distributions of Richardson number are calculated as functions of depth. Finally, we close with a discussion (section 4) and conclusion (section 5).

2. Methods

The goals of ROGER were addressed through repeated deployments of Spray underwater gliders (Sherman et al. 2001) on three lines. The central line was on 93°W between 2°S and 2°N, where the objective was to have two gliders on this line at all times. In addition, two lines from the northern and southern ends of the Galápagos archipelago (at Isla Isabela) to the ends of the 93°W line were designed to close off a box for the
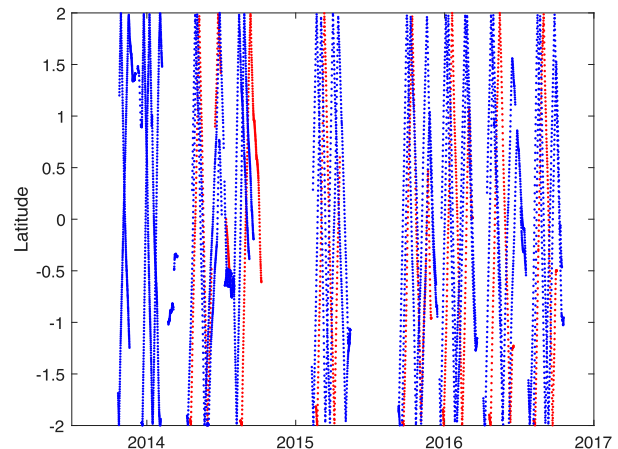
calculation of budgets (Jakoboski et al. 2020). A companion project, "Modernizing the tropical ocean/atmosphere observing system," funded a glider on 95°W where the westernmost TAO line is located. The full glider network was thus intended to include five gliders surveying at all times. A total of 3014 glider-days of data were collected, with gliders covering 53 463 km over ground and 57 406 km through water in 12 836 dives (Fig. 1).

This observing campaign proved challenging to maintain in totality, but the occupations on 93° and 95°W were reasonably well sustained (Fig. 2). On 93°W, 6346 dives were within 60 km of the desired line, and on 95°W 1831 dives were on the line. Coverage on 93°W improved over the first year of occupation during October 2013–October 2014 until a break at the end of 2014. Another break in coverage over a few months in 2015 was followed by fully sustained observations during September 2015–October 2016. Sampling on 95°W started later in April 2014 and then followed the same pattern as on 93°W.

The Spray gliders were equipped with a complete suite of sensors for observing physical processes. The pumped Sea-Bird CTD was plumbed into a Seapoint fluorometer, sampling temperature, salinity, pressure, and chlorophyll fluorescence at 8-s intervals during ascent. Two models of ADCP were used during the experiment. The project started with 750-kHz Sontek ADPs. Unfortunately, the limited 500-m depth range of the Sontek was too shallow to escape the strong biofouling in the euphotic zone of this productive region. We changed to 1-MHz Nortek AD2CPs after the first few missions. The 1000-m capability of the Nortek allowed the glider to profile deep enough to slow biofouling such that 100-day missions were achievable.

In typical operation, the Spray gliders profiled from the surface to 1000 m and back in about 6 h, covering roughly 6 km in the horizontal during that time. The gradual growth in biofouling increased drag during a mission, lengthening the time for a dive, and affecting flight especially through increased angle of attack. ADCP data processing was done as described

in Todd et al. (2017), including an estimation of increasing angle of attack. Absolute velocity profiles were calculated by combining shear from the ADCP with depth-average velocity estimated using measurements of glider pressure, heading, and pitch (Rudnick et al. 2018). Measurements from the CTD and ADCP were averaged in common 10-m depth bins over the upper 1000 m for each dive, forming the dataset for all subsequent calculations.

A well-known feature of all finite-time oceanic surveys, including by gliders, is a projection of temporal variability into spatial variability (Garrett and Munk 1972). Past studies in midlatitudes have suggested that wavenumber spectra from gliders were affected by this projection at wavelengths shorter than about 30 km (Rudnick and Cole 2011). Spectra of eastward velocity were calculated on several depth surfaces (Fig. 3) to see this effect in the ECS where the inertial frequency approaches zero. As in Rudnick et al. (2017), the spectra were calculated as functions of frequency (bottom axis of Fig. 3) by averaging over chunks of data 80 dives (roughly 20 days) long. The equivalent wavenumber is estimated using the average speed the glider makes in the meridional direction of $0.20\,\mathrm{m\,s^{-1}}$ (upper axis of Fig. 3). Similar to previous results, a minimum in the spectra near 0.03 cycles per kilometer suggests that wavelengths shorter than 30 km may be contaminated by projection of high-frequency variability. Thus, 30 km is an appropriate length scale for the objective maps discussed below. The spectrum grows toward high frequency where variability due to tides and internal waves exists. The increase toward low frequency may then be representative of the 20-day variability present in the ECS (Legeckis 1977).

An analysis goal was to create maps of observed variables as functions of depth, latitude and time on each of the lines. This mapping was achieved following methods used to create a climatology on glider lines in the California Current System (Rudnick et al. 2017). In particular, mean fields on each line were calculated by a weighted least squares fit, and objective maps were calculated on each depth surface as functions of distance along the line and time. The least squares fit was done at 0.05° intervals in latitude along each longitudinal line, using a Gaussian window with an *e*-folding length scale of 15 km. The objective map was performed on anomalies from the mean fields, calculated on a grid of 0.05° latitude by 10 days. A Gaussian autocovariance was used in the objective map with *e*-folding scales of 30 km and 60 days, and an uncorrelated noise of 0.1 times the signal variance. The *e*-folding length scale was motivated by the results of the spectral analysis, as discussed in the previous paragraph (Fig. 3). The 60-day time scale provides some additional smoothing given the roughly 25 days it took to complete a section. The choices of length and time scales are identical to those in Rudnick et al. (2017), where additional details on the method can be found. Objective maps provide a measure of error, and we masked the maps wherever the ratio of error-to-signal variance was greater than 0.1. Mapped variables included temperature, salinity, and eastward and northward velocities. Variables derived from these maps included density, potential density, and potential temperature. The maps allowed gradients to be calculated self-consistently
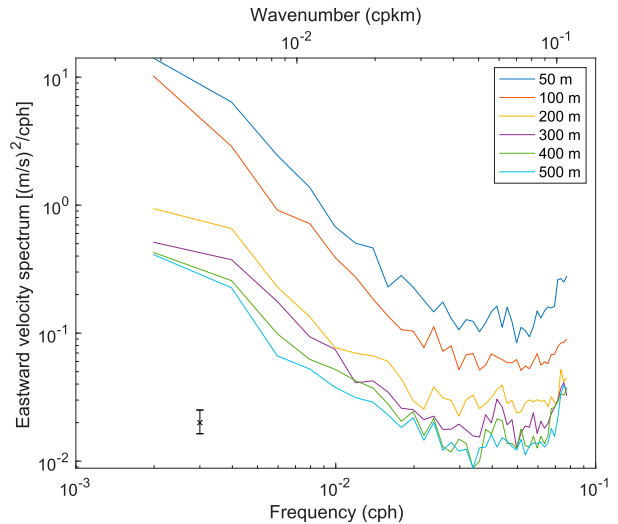

FIG. 3. Spectra of eastward velocity at several depths on 93°W. The spectra are calculated as functions of frequency in cycles per hour (cph), and the equivalent wavenumber is shown on the upper axis in cycles per kilometer (cpkm). The 0.9 confidence interval is indicated by the black cross and whiskers. Note the minimum near 0.03 cph or cpkm.

using centered differences on the grid 10 m in depth by 0.05° in latitude by 10 days in time, and potential vorticity and Richardson number to be estimated.

3. Results

The presentation of results starts with a thorough description of the mean fields of potential temperature, salinity, potential density, and eastward and northward velocity. The derived variables potential vorticity and Richardson number are examined. Notable results include structure in the mean gradients at the resolved scales of tens of kilometers in the horizontal and 10 m in the vertical. We then address the variability over the 3 years including the establishment and breakdown of El Niño conditions. An objective is to describe the temporal evolution over the 3-yr period as functions of latitude and depth. Time series indices of temperature, salinity, eastward velocity, and isopycnal depth are used in a correlation analysis to address the effects of horizontal and vertical advection. Finally, distributions of Richardson number are presented as a function of depth.

a. Mean

The observations on 93°W provide finely spatially resolved temporal-mean fields. The mean potential temperature (Fig. 4a) is highly stratified at the surface, especially north of the equator where a strong meridional gradient exists. Salinity (Fig. 4b) shows a striking pattern of high values to the south of the equator at about 70-m depth in a subsurface salinity maximum, and a near-surface fresh layer to the north of the equator associated with freshwater flux under the ITCZ. The mean meridional gradients of temperature and salinity at the surface are a manifestation of the oceanic equatorial front. The EUC is the
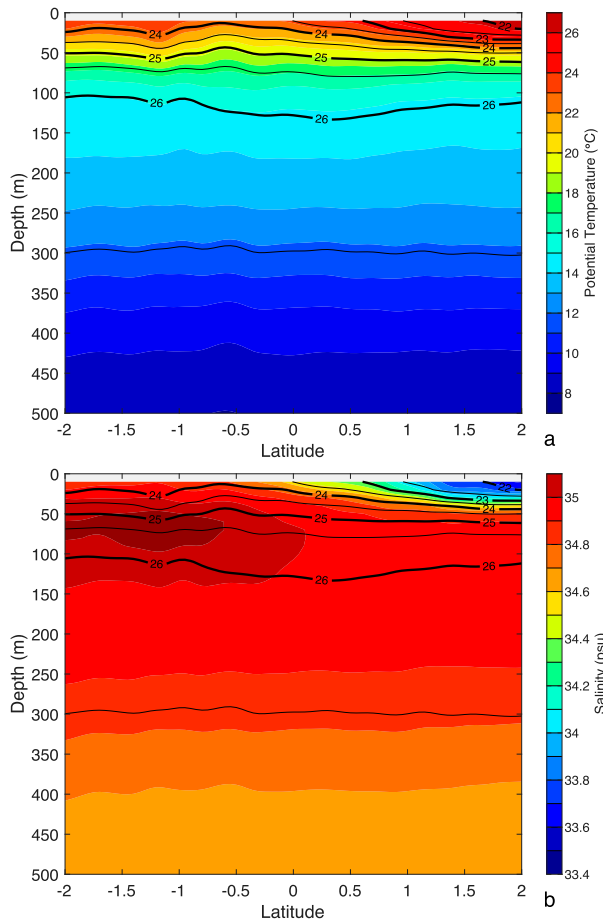
FIG. 4. Mean (a) potential temperature and (b) salinity (color shading) and potential density (black contours) on 93°W.

FIG. 5. Mean (a) eastward and (b) northward velocity (color shading) and potential density (black contours) on 93°W.

dominant feature of mean eastward velocity (Fig. 5a), strongest at roughly 75-m depth at a latitude of about −0.25°. The EUC is accompanied by a broadening of the potential density contours. Above and especially to the north of the EUC lies the westward SEC. The strain between these two currents is responsible for the striking salinity pattern including the warm freshwater near the surface to the north and the high salinities penetrating in the EUC. An important feature is the meridional gradient of salinity in the EUC, with saltier water to the south. This gradient of salinity across the EUC suggests that the current derives from distinct water masses further to the west (e.g., Johnson and McPhaden 1999). The meridional velocity (Fig. 5b) is strongly divergent, with northward flow to the north of the equator, and southward flow to the south. This pattern of divergence is strongest in the upper 200 m, and weakens down to 500 m. The implication of this one-dimensional divergence is that there must be two-dimensional convergence in the zonal and vertical directions, consistent with the general anatomy of the subtropical cells (Capotondi et al. 2005). Slowing of the EUC and upwelling near the Galápagos Islands to the east are understood from ocean models (Eden and Timmermann 2004; Karnauskas et al. 2007). For a rough notion of the order of magnitude if there were no
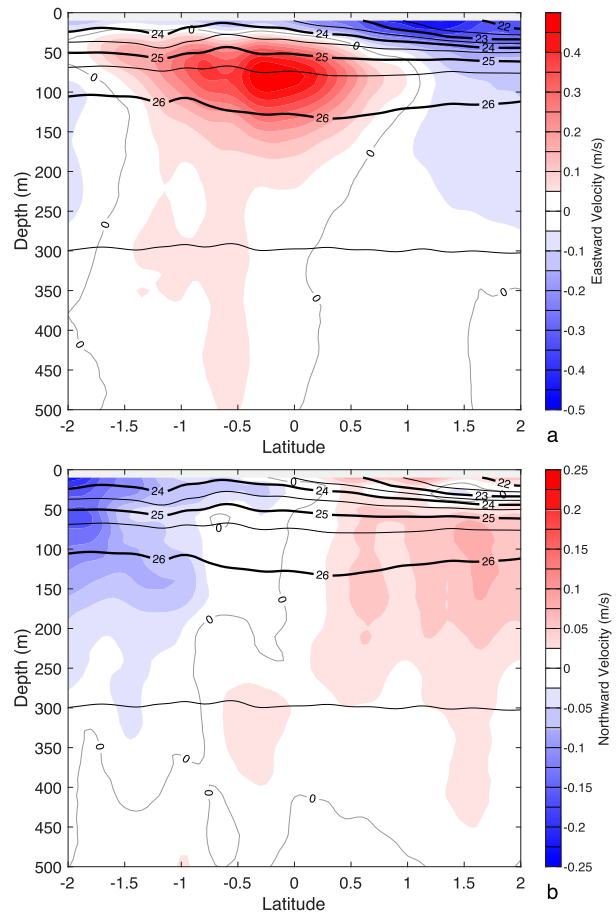
zonal convergence, the mean meridional divergence implies upwelling of about 10 m day^{-1} at a depth of 500 m. An analysis of the volume budget using the diagonal tracks connecting ±2°N to the Galápagos has been done by Jakoboski et al. (2020), where an upwelling velocity of 8 m day^{-1} was found.

Variance caused by tropical instability waves (TIWs) is a likely source of error in the mean fields. To evaluate the effects of TIWs, we assume an independent observation is produced every 20 days (roughly the time required for a glider to complete a section) so that we have 36 samples. In our data the maximum standard deviation in eastward velocity is 0.4 m s^{-1} (found near the top of EUC), consistent with values reported for TIWs (Jochum and Murtugudde 2006). This yields an upper-bound estimate of the standard error of the mean of $0.4/\sqrt{36} = 0.07$ m s^{-1}. With this standard error, the major features of the ECS are resolved (Fig. 5a).

The strong gradients in the mean velocity and density fields have striking effects on the dynamical tracer potential vorticity Q (Gill 1982). The structure of Q is useful to diagnose the necessary conditions for instability, either through changes in the sign of Q or changes in the gradient of Q. Given the mean meridional sections of potential density and velocity, potential vorticity is estimated as

$$Q = -\frac{1}{\rho_0}\left[\left(f - \frac{\partial u}{\partial y}\right)\frac{\partial \rho_\theta}{\partial z} + \frac{\partial u}{\partial z}\frac{\partial \rho_\theta}{\partial y}\right], \quad (1)$$

where f is the Coriolis parameter, u is eastward velocity, ρ_θ is potential density, ρ_0 is a reference density, and y and z are northward and vertical position. The horizontal component of planetary vorticity is not included as it is negligible relative to the horizontal component of relative vorticity $\partial u/\partial z$. This approximation of Q neglects eastward gradients of velocity and potential density. The magnitude of the peak observed eastward gradient of mean potential density (between 93° and 95°W) is one-tenth the magnitude of the peak northward gradient of mean potential density, supporting this approximation. Potential vorticity [Eq. (1)] is defined with a negative sign so that Q has the same sign as f when velocity is negligible. In such a state of no flow, Q would have the largest magnitudes where stratification is strongest and would change sign at the equator. The observed mean Q (Fig. 6a) is indeed positive north of the equator, and mostly negative to the south. A notable exception to this pattern is a region of positive Q above and to the south of the core of the EUC. This change in sign satisfies the formal conditions for symmetric instability (Hoskins 1974), and the many changes in the sign of the gradient of Q implies that baroclinic instability is also possible (Gill 1982). The cause of this region of positive Q in the Southern Hemisphere is an increase in the term involving the product of the vertical shear of eastward velocity and the northward gradient of potential density [Eq. (1)]. To be clear, this Q of opposite sign to planetary vorticity is caused by the mean fields of velocity and density. The term involving the vertical component of relative vorticity mostly serves to supplement planetary vorticity as the EUC is cyclonic on its northern and southern edges as the current spans the equator in the mean.

The high mean shear on the lower and upper edges of the EUC suggest the possibility of strong mixing. To quantify this potential for mixing, we calculate the Richardson number defined as

$$\text{Ri} = \frac{N^2}{\left(\frac{\partial u}{\partial z}\right)^2 + \left(\frac{\partial v}{\partial z}\right)^2}, \quad (2)$$

where v is northward velocity and the buoyancy frequency squared is

$$N^2 = -\frac{g}{\rho_0}\frac{\partial \rho_\theta}{\partial z}. \quad (3)$$

As a state of zero shear leads to infinite Ri, the quantity $\tan^{-1}\text{Ri}$ is calculated so that the range of Ri from zero to infinity is mapped onto angles from 0° to 90°. The observed $\tan^{-1}\text{Ri}$ approaches 45° (Ri = 1) in the high shear regions above and below the EUC (Fig. 6b). In general, values of Ri near unity suggest that mixing may be important, although the intensity of turbulence may depend on additional factors (Zaron and Moum 2009).

The low values of Ri and likely strong mixing in the EUC are relevant to the interpretation of Q as a tracer. As with all
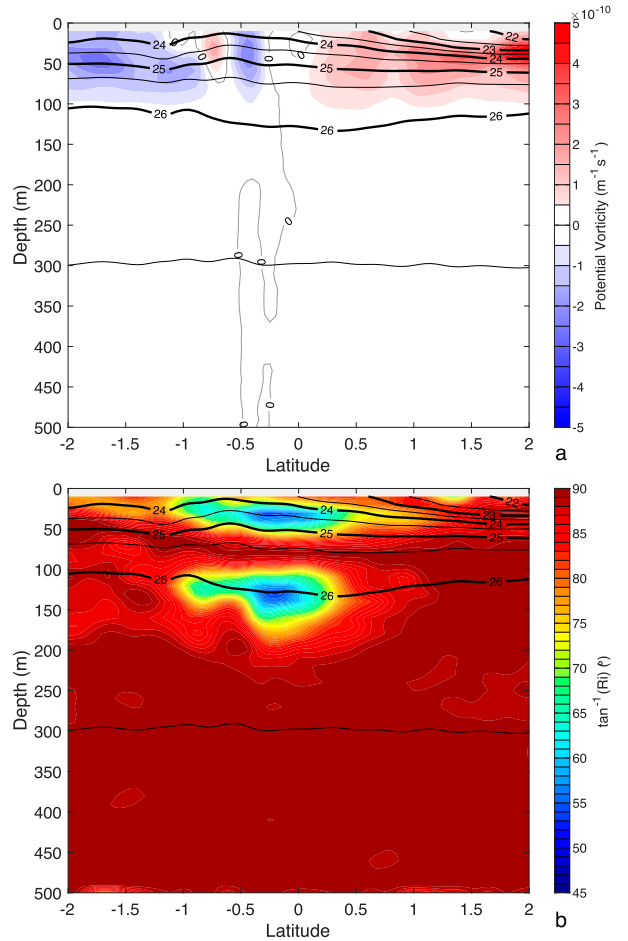

FIG. 6. Mean (a) potential vorticity and (b) the inverse tangent of the Richardson number (color shading) and potential density (black contours) on 93°W.

conserved tracers, Q is strictly conserved only when mixing is negligible. In addition, the very existence of a patch of positive Q where the planetary vorticity is negative depends on Ri being low. This can be understood by rewriting the potential vorticity in terms of the Rossby number Ro, here defined as the vertical component of relative vorticity divided by the planetary vorticity

$$\text{Ro} = \frac{-\frac{\partial u}{\partial y}}{f} \quad (4)$$

and the geostrophic Richardson number

$$\text{Ri}_g = \frac{N^2}{\left(\frac{\partial u_g}{\partial z}\right)^2}. \quad (5)$$

Here, the geostrophic velocity u_g obeys the thermal wind equation

$$f\frac{\partial u_g}{\partial z} = \frac{g}{\rho_0}\frac{\partial \rho_\theta}{\partial y}, \quad (6)$$

where g is gravitational acceleration. A further assumption in Eq. (6) is that the meridional gradient of density may be approximated by the meridional gradient of potential density, which is reasonable near the surface as in these observations. The resulting approximation for potential vorticity is

$$Q_g = \frac{fN^2}{g}(1 + \text{Ro} - \text{Ri}_g^{-1}). \tag{7}$$

This expression for Q_g makes clear the effect of low Richardson number to change the sign of potential vorticity. As low Richardson number is also associated with increased mixing, the notion of conserving potential vorticity deserves scrutiny given the strong observed gradients at the equator. Finally, we note that the thermal wind as written in Eq. (6) certainly fails close to the equator, but the shear is at least partially geostrophically balanced (Lukas and Firing 1984; Lagerloef et al. 1999), and Eq. (7) is useful to understand the relationship between Ri and potential vorticity.

The mean temperature and salinity at 95°W (Fig. 7) show similar features as at 93°W. The eastward difference in mean potential temperature is calculated as $\theta = \theta(93°W) - \theta(95°W)$, where the subtraction is done on depth surfaces (Fig. 8a). The upper 100 m is cooler on 93°W, consistent with shoaling of the thermocline to the east. There is a slight tendency toward warming near 200 m, indicative of an eastward deepening of isotherms in this more weakly stratified region. The difference in salinity between the two sections is calculated on isopycnals (Fig. 8b). The dominant feature is a freshening toward the east in the upper north corner of the section where the SEC advects freshwater westward (Figs. 4b and 5a). This weakening of the salinity minimum in the westward direction is consistent with a source of freshwater to the east. This fresh eastward difference appears at the surface across the sections, coincident with shallow westward flow at 93°W (Fig. 5a). The mean at 95°W is computed over 29% as many dives as at 93°W (Fig. 2), so the eastward differences may be influenced by the different time periods sampled on the two sections. However, the fundamental results of shoaling of the isotherm to the east and westward advection of freshwater are likely robust (Johnson et al. 2002).

b. Variability

The observations collected during ROGER fortuitously allow a description of variability during the 2014–16 El Niño. This description begins with the temperature and zonal wind along the equator and then focuses on the glider observations at 93°W. The mapped variables are functions of depth, latitude and time, so they may be examined through slices in any of these dimensions. Variability is discussed through plots of vertically averaged variables as functions of time and latitude, and of meridionally averaged variables as functions of time and depth. Indices of temperature, isopycnal depth, salinity, and eastward velocity are created by averaging in depth and latitude, and the resulting time series are used to address vertical and horizontal advection. Example sections during times of extrema are examined. Finally, statistical distributions of the
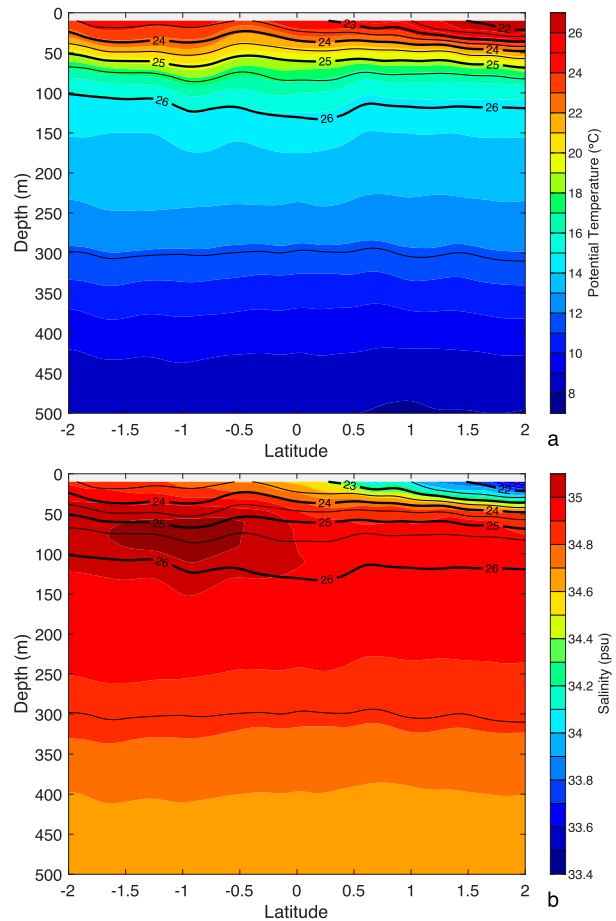

FIG. 7. Mean (a) potential temperature and (b) salinity (color shading) and potential density (black contours) on 95°W.

Richardson number are constructed to assess the importance of mixing as a function of depth.

1) TEMPERATURE AND ZONAL WIND

The temperature and zonal wind along the equator reveal the evolution of the 2014–16 El Niño. The temperature averaged over the upper 300 m and in the latitude range ±5°N (Fig. 9a) is from the Roemmich–Gilson Argo climatology (Roemmich and Gilson 2009). The monthly values of temperature are anomalies relative to the annual cycle from 2004 until 2017. The 10-m zonal wind (Fig. 9b) is from the NCEP–NCAR reanalysis (Kalnay et al. 1996), with daily values averaged in the latitude range ±5°N. The first indication that an El Niño was incipient was in late 2013 through early 2014 when anomalously warm water began to appear in the western equatorial Pacific (Fig. 9a). This warming was accompanied by westerly wind bursts in early 2014 in the longitude range 140°–160°W (Fig. 9b). A warm (downwelling) Kelvin wave swept across the Pacific in early 2014 prompting some forecasts of an incipient El Niño (McPhaden 2015). This rapid march toward an El Niño slowed in mid-2014, with westerly winds receding in the western Pacific and a cool (upwelling) Kelvin wave appearing (Hu and Fedorov 2017). Some of this warm
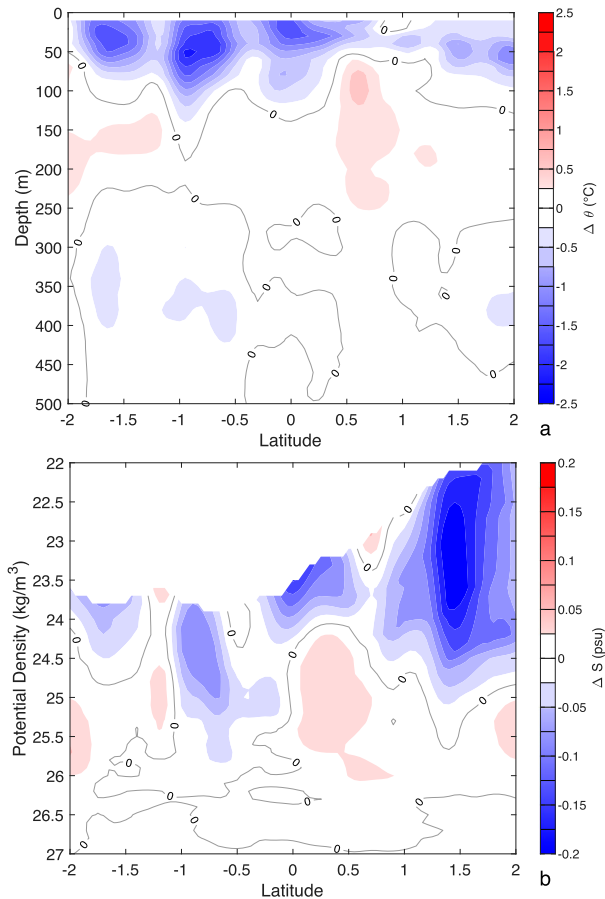
FIG. 8. The eastward difference between mean sections on 93°
and 95°W of (a) potential temperature calculated on depth surfaces
and (b) salinity calculated on potential density surfaces. The dif-
ference is calculated as the values at 93°W minus those at 95°W.
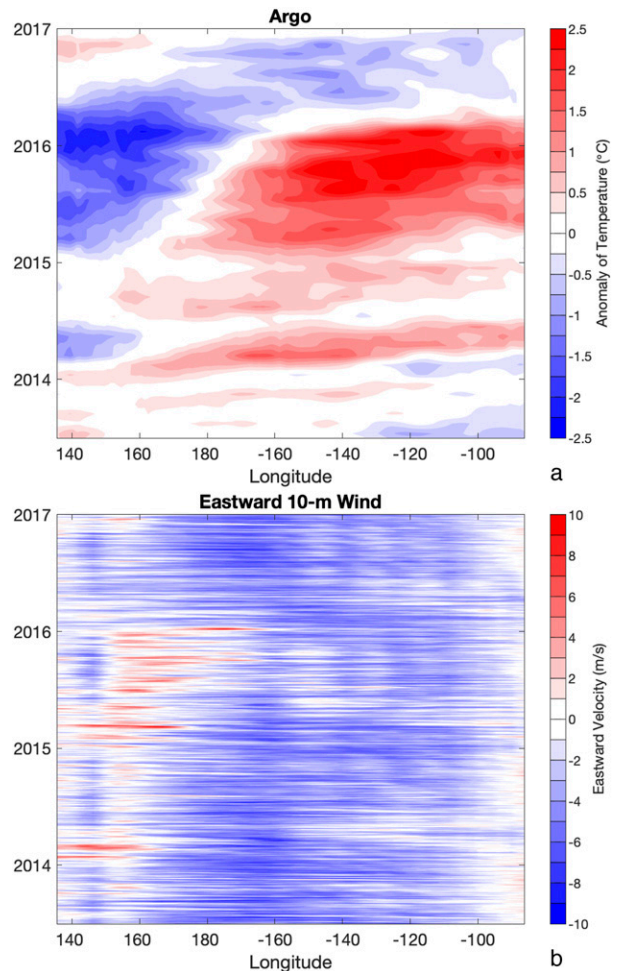

FIG. 9. (a) Temperature anomaly in the upper 300 m and (b)
eastward 10-m wind averaged within the latitude band ±5°. The
temperature anomaly is monthly relative to the annual cycle since
the year 2004, derived from the Roemmich–Gilson Argo clima-
tology. The wind is daily from the NCEP–NCAR reanalysis.

water remained, and further warming began again in early
2015. Sustained westerly winds and a series of warm Kelvin
waves throughout 2015 ultimately caused the strongest El Niño
since 1997/98. At the height of the El Niño event, temperature
anomalies approached 2.5°C in the vicinity of the Galápagos
Islands and the site of ROGER observations. As is the case in
much of the tropics, the El Niño signal is much larger than the
annual cycle, which has an amplitude of less than 1°C averaged
over the upper 300 m of this region (Gasparin and Roemmich
2017). The El Niño waned in 2016, with a very weak La Niña
following.

2) VARIABILITY AS FUNCTION OF TIME AND LATITUDE

The evolution of the 2014–16 El Niño may be examined
through the potential temperature and salinity averaged over
the upper 300 m (Fig. 10). The vertical average shown includes
values in 10-m bins centered between 10 and 300 m. Therefore
the vertical average includes data as shallow as 5 m and as
deep as 305 m. A reason to consider the upper 300 m is for
consistency with the weekly ENSO update prepared by NCEP.
The warming during the first half of 2014 is followed by a rapid

cooling in mid-2014. Warming recommences in early 2015 and
remains until spring 2016 spanning the peak of the El Niño.
Warming extended throughout the observed latitude range of
±2°. The end of the El Niño during 2016 is marked by rapid
cooling. Salinity is distinguished by a series of salty pulses
throughout the record with the first pulse in 2014 concurrent
with the dramatic warming at that time. Later salty pulses in
2015–16 are not all accompanied by warming. The salty pulses
were especially strong south of the equator, with a meridional
gradient of salinity apparent throughout the record. The
equatorial front separates freshwater to the north from salty
water further south; the southward penetration of freshwater
indicates the southward shift of the equatorial front. An es-
pecially fresh event occurred near the change of the calendar
year 2015–16 and was strongest at 2°N. This fresh anomaly has
been noted in Argo data and was attributed to precipitation
and zonal advection (Gasparin and Roemmich 2016). By the
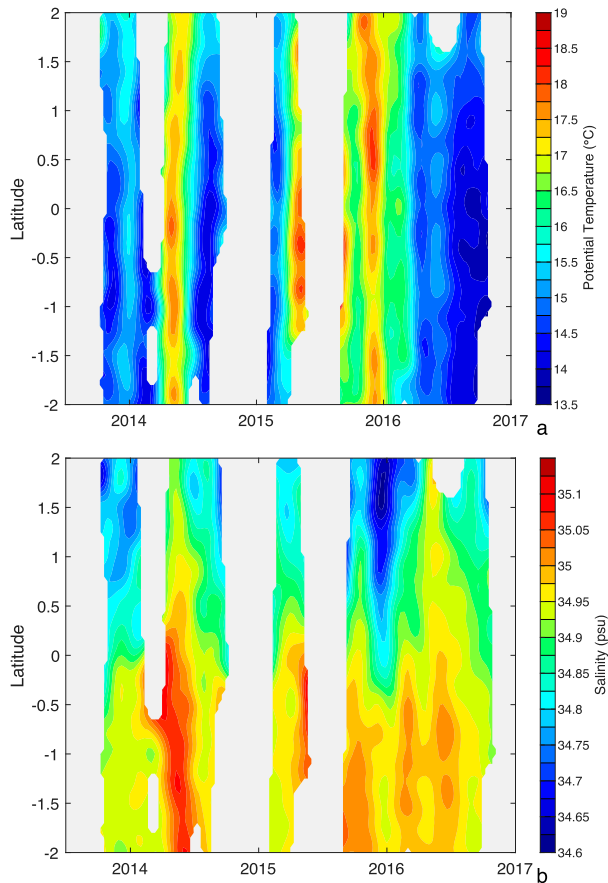end of the record, the highest salinities are no longer apparent,

FIG. 10. (a) Potential temperature and (b) salinity averaged in the range 10–300 m as a function of time and latitude on 93°W.

FIG. 11. (a) Eastward and (b) northward velocity averaged in the range 10–300 m as a function of time and latitude on 93°W.

but the cooling in mid-2016 is not accompanied by a similarly abrupt decrease in salinity. The differences in the temperature and salinity fields is a central result of these high-resolution observations.

The zonal and meridional velocity, averaged over the upper 300 m (Fig. 11), show the evolution of the EUC during the El Niño. The EUC flows eastward throughout the 3 years of observation, with a series of pulses. Comparing zonal velocity (Fig. 11a) with temperature (Fig. 10a) suggests that the pulses in velocity are not coincident with periods of high temperature. However, the eastward pulses do have a relationship with times of high salinity (Fig. 10b) south of the equator (Lukas 1986). The coincidence between salinity and eastward velocity is not perfect, and velocity leads salinity for some events. If high salinity is primarily coming from the west, then this leading eastward velocity is expected. A correlation analysis below shows that eastward velocity leads salinity by 30 days. The SEC is characterized by westward flow typically north of 1°N. This westward flow is present much of the time, although it is pushed northward during times when the EUC is especially broad. The tendency for northward velocity (Fig. 11b) north of the equator, and southward velocity to the south is clear throughout the record. Thus, the mean meridional divergence (Fig. 5b) is a fair representation of conditions that are often
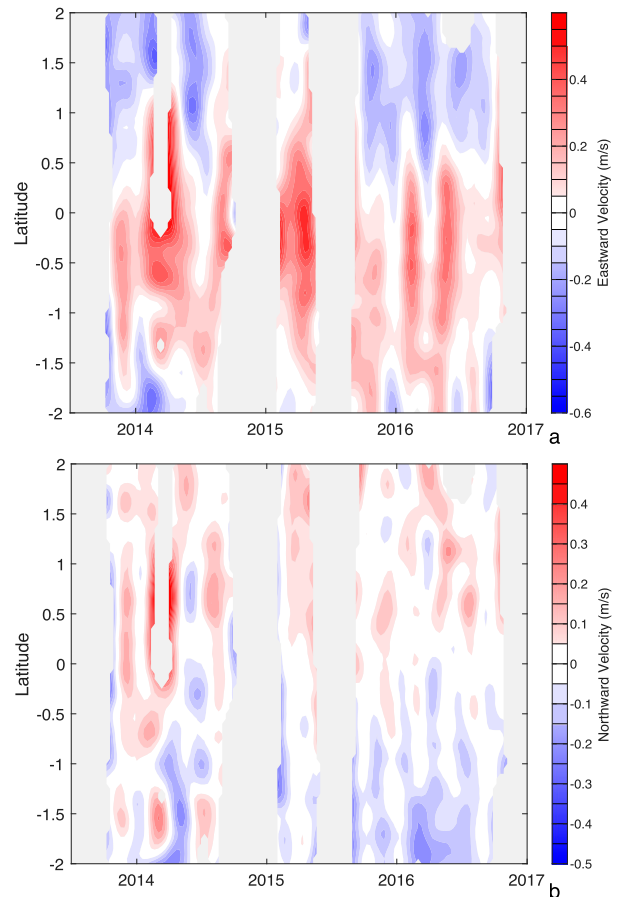
present, rather than being dominated by a few events. There is no obvious relationship between variations of northward velocity and any of the other observed variables. In summary, the persistence of the EUC and meridional divergence is a fundamental result, as is the relationship between pulses in eastward velocity and salinity.

3) VARIABILITY AS FUNCTION OF TIME AND DEPTH

To examine the structure of the variability as a function of depth, the potential temperature and salinity are averaged in the range 2°S–1°N (Fig. 12). This latitude range is chosen as it spans the EUC in the mean (Fig. 5a), so the resulting fields should be affected by fluctuations in the EUC. Periods of high temperature (Fig. 12a) are seen to be coincident with depressions of isopycnals. Thus, the periods of high temperature are likely caused by downwelling, although this downward motion may have occurred further upstream to the west rather than by local processes. That the warm periods are a result of downwelling may explain why there is no obvious correlation between pulses in the EUC and high temperatures, as discussed above. The highest salinities (Fig. 12b) seem to ride near the $25 \, \mathrm{kg \, m^{-3}}$ isopycnal, with fluctuations in the size of this local maximum throughout the record. The fresh anomaly located
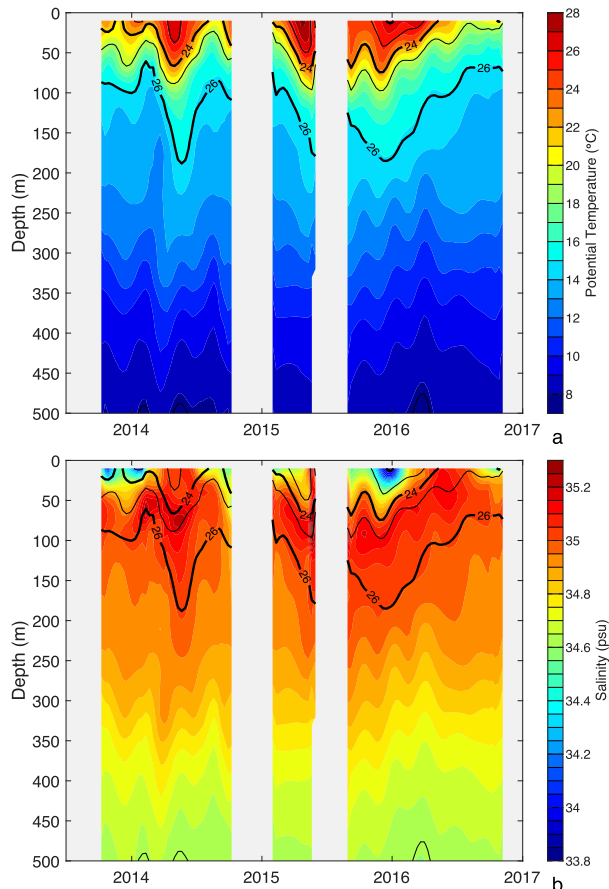
FIG. 12. (a) Potential temperature and (b) salinity averaged in the range 2°S–1°N as a function of time and depth on 93°W. Black contours are isopycnals.
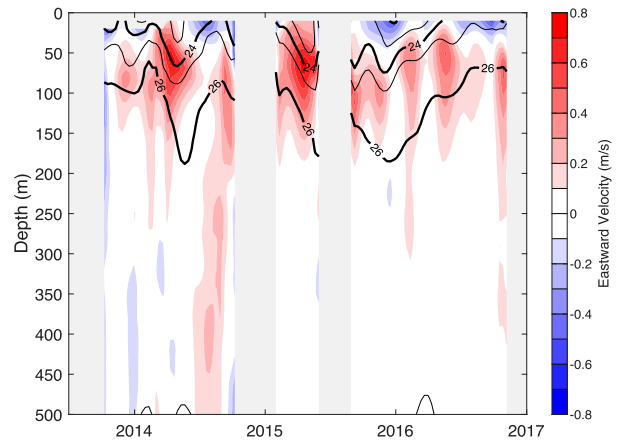

FIG. 13. Eastward velocity averaged in the range 2°S–1°N as a function of time and depth on 93°W. Black contours are isopycnals.

4) TIME SERIES INDICES

To understand the effects of vertical and horizontal advection on temperature and salinity, indices of temperature, isopycnal depth, salinity and eastward velocity are presented. A standard index of El Niño is the oceanic Niño index (ONI), the sea surface temperature in the Niño-3.4 region (5°N–5°S, 170°–120°W) filtered with a 3-month running mean (Fig. 14a). For comparison, all indices to follow are filtered with a 90-day running mean. First, consider potential temperature averaged over the upper 300 m and the depth of the 26 kg m⁻³ isopycnal, both averaged between 2°S and 1°N (Fig. 14b). These two indices are highly correlated, with a correlation coefficient of $r_{\theta h} = 0.95$. Taking the isopycnal depth to be a proxy for vertical displacement, it is reasonable to conclude that temperature is strongly affected by vertical advection. The highest temperatures observed by the gliders were in mid-2014 and in late 2015 (Fig. 14b), corresponding to maxima in the Argo data (Fig. 9a) at 95°W. The propagating maxima in the Argo data were caused by baroclinic Kelvin waves, whose linear temperature balance involves only vertical advection (Gill 1982). A plausible interpretation is that changes in temperature observed by gliders at 93°W are due to vertical heaving by propagating Kelvin waves.

Next consider indices of salinity and eastward velocity. Salinity is averaged over the upper 300 m and between 2°S and 1°N, and eastward velocity is integrated over the same region to yield transport in units of Sverdrups (Sv; $1\,\mathrm{Sv} \equiv 10^6\,\mathrm{m}^3\,\mathrm{s}^{-1}$). These indices have a correlation coefficient $r_{Su} = 0.58$ at zero lag, with an even higher $r_{Su30} = 0.83$ with eastward velocity leading salinity by 30 days. This relationship with eastward velocity leading salinity is apparent in the extrema of the two indices. Velocity leading salinity is evidence but not proof that salinity changes are caused by eastward advection.

The correlation coefficients between temperature and isopycnal depth, and between salinity and eastward velocity are statistically significant. We evaluate significance through the 95% confidence interval, conservatively assuming one independent

north of the equator at the end of 2015 (Fig. 10b) is seen to be a surface trapped feature (Fig. 12b). This depth structure of temporal fluctuations demonstrates that the maxima of temperature are at the surface, while the maxima of salinity are in the pycnocline.

Zonal velocity is similarly averaged between 2°S and 1°N (Fig. 13). The EUC is strongest in the pycnocline, often in the range 24–25 kg m⁻³, and the depth of maximum velocity tends to follow the excursions of the pycnocline. There are a series of eastward pulses in time which are not obviously related to the fluctuations in pycnocline depth, although the two strongest pulses co-occur with isopycnal depressions. The pulses of eastward velocity (Fig. 13) and salinity (Fig. 12b) are clearly largest in the pycnocline, supporting the notion that high salinity is advected from the west (Lukas 1986). Even so, the coincidence between maxima in eastward velocity and salinity is not perfect. The fresh surface anomaly at the end of 2015 corresponds with a surface westward flow, again suggesting an advective component to salinity evolution. Taken together, these results suggest that temperature is strongly affected by vertical advection, while salinity may depend more on horizontal advection.
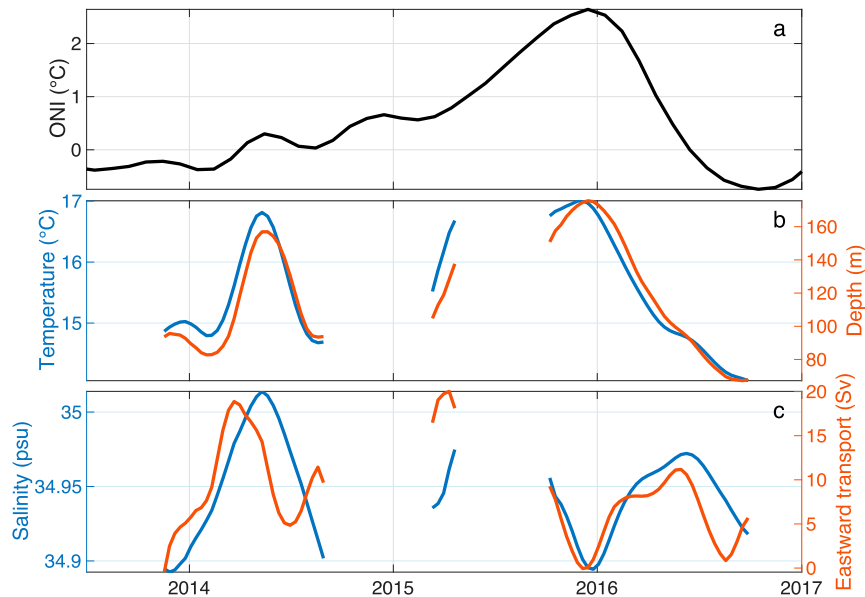
FIG. 14. (a) The ONI, (b) potential temperature averaged in the upper 300 m and over the range 2°S–1°N and the depth of the 26 kg m^{-3} isopycnal averaged over 2°S–1°N, and (c) salinity averaged in the upper 300 m and over the range 2°S–1°N and eastward transport (Sv) in the upper 300 m and between 2°S and 1°N . The ONI is the Niño-3.4 measure of sea surface temperature filtered with a 3-month running mean. Accordingly, each of the time series in (b) and (c) are filtered with a 90-day running mean.

sample every 90 days, consistent with the 90-day running mean applied to the data. Given our 2 years of data, we thus assume there to be eight independent samples. The confidence interval of r_{Su30} is 0.29–0.97, and of r_h is 0.76–0.99, indicating that both correlation coefficients are statistically significant. The 95% confidence interval of r_{Su} overlaps with zero, but r_{Su} is formally significant at the 86% level. None of the correlation coefficients between other pairs of indices in Fig. 14 are statistically significant.

5) SECTIONS DURING TIMES OF EXTREMA

A central result is that temperature and pycnocline depth are correlated, as are salinity and eastward velocity, but that these pairs are not correlated with each other. An examination of sections during times of extrema in these variables is useful. The analysis above showed that periods of anomalous warmth coincide with a deep pycnocline, while cool periods occur when the pycnocline is shallow; perhaps an obvious correlation. Less plainly obvious is a correlation between salinity and eastward velocity such that a strong EUC accompanies high salinity while weak eastward flow corresponds to fresh periods. Times of warm, deep pycnoclines (left column, Fig. 15) occur near the beginning of the El Niño and at its peak. During April 2014 this warmth is accompanied by a strong EUC and salty conditions, while in December 2015 the EUC is weak and the water is fresh. Periods of cool, shallow pycnoclines (right column, Fig. 15) occur during the waning of the El Niño and before the El Niño. The EUC is strong with salty water in June 2016, while the EUC is relatively weak and fresh during December 2013. Times of weak EUC (bottom row, Fig. 15) also have a strong

SEC extending southward and bringing relatively freshwater, while a strong, wide EUC tends to push the SEC northward. These combinations of extrema emphasize that temperature and salinity have different drivers in this region of the equatorial Pacific.

6) DISTRIBUTION OF RICHARDSON NUMBER

The regions of strong shear at the top and bottom of the EUC lead to low Richardson numbers, and possibly important mixing. The Richardson number is low even when calculated from the mean density and velocity fields (Fig. 6b), similar to the frequently near-critical values (Ri = 1/4) observed at 140°W above the EUC (Moum et al. 2009). Because shear can be intermittent, maps of Ri are difficult to interpret, and we instead calculate the probability density function of $\tan^{-1}$Ri as a function of depth (Fig. 16). Shear and buoyancy frequency [Eqs. (2) and (3)] are calculated from the raw data binned at 10-m intervals using a centered difference to estimate the vertical derivatives. The resulting profiles of Ri are then used to create probability density functions of $\tan^{-1}$Ri at 10-m intervals in the upper 200 m. The shallowest depth analyzed, at 10 m, has a mode between 15° and 35° where Ri ranges between 0.3 and 0.6. This low Ri is caused by low stratification in the mixed layer and high shear at the top of the EUC. Strong mixing in this region is understood. At all depths below 10 m, the mode of $\tan^{-1}$Ri is at 90°. However, a second region of high shear occurs at the base of the EUC near 100-m depth. Values of $\tan^{-1}$Ri near 45° are more likely in this region, indicating a Ri near unity. The increased likelihood of low Ri at these depths near 100 m can also be seen in Fig. 16 by the reduction of the mode at 90° near 100 m. This deep region of strong mixing is a
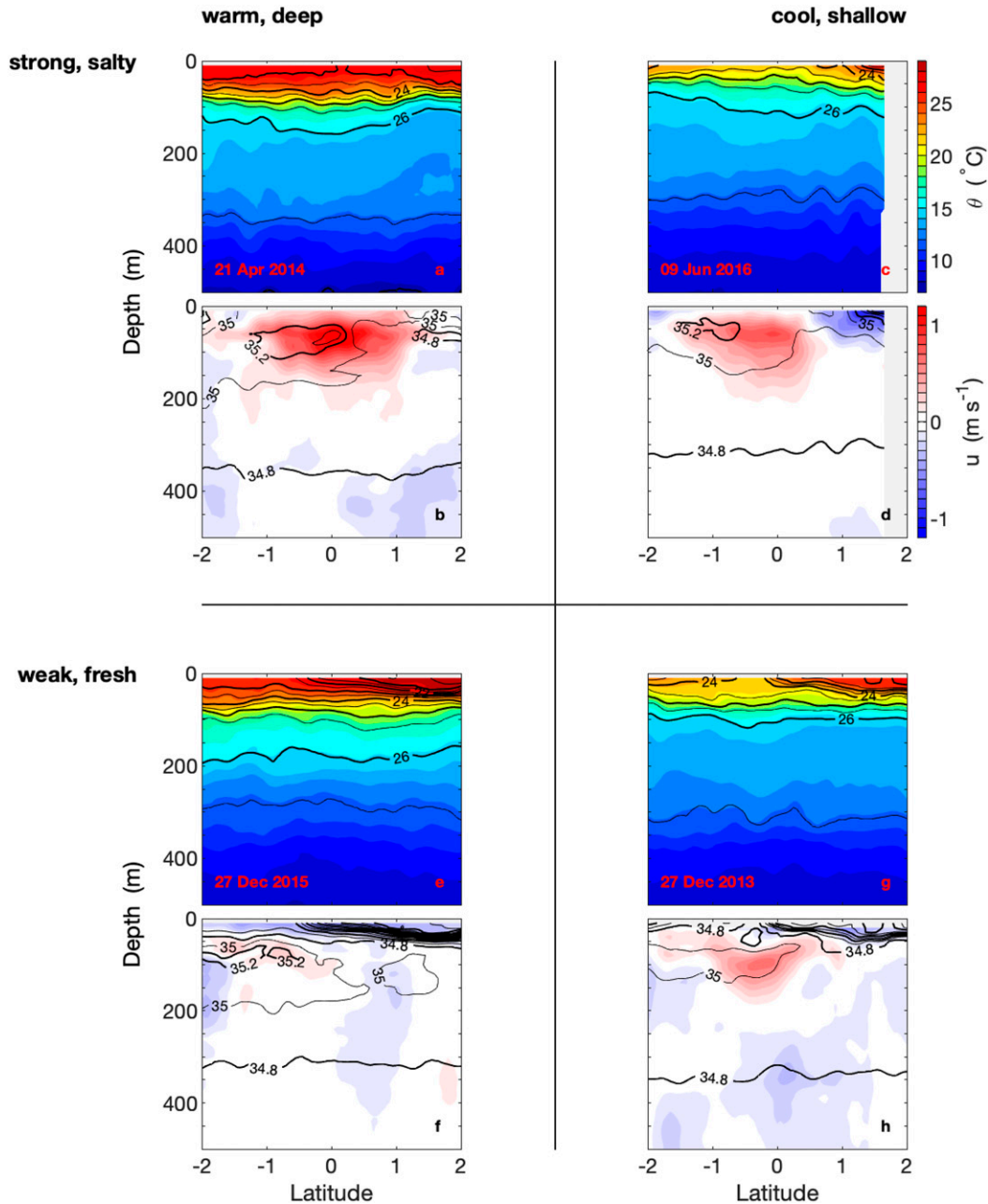
warm, deep

cool, shallow

strong, salty

FIG. 15. (a),(c),(e),(g) Sections of potential temperature (color shading) and potential density (black contours) and (b),(d),(f),(h) eastward velocity (color shading) and salinity (black contours). The date of each section is written in the lower left-hand corner of the potential temperature section. Shown are all possible extremes of these pairs of correlated variables. Warm temperature and deep pycnocline is in the right column, with cool and shallow in the left column. Strong eastward flow and salty is in the upper row, with weak flow and fresh in the lower row.

unique feature of the EUC, with effects that may be relevant to equatorial circulation.

4. Discussion

The mean fields derived from the glider data are distinguished by their fine horizontal resolution. The ability to sustain fine spatial resolution is a unique feature of observations by underwater gliders and is the fundamental advance relative to the seminal work of Johnson et al. (2002). Notable features in the mean are strong spatial gradients within the EUC, the equatorial front at the surface, and the strong gradient in salinity across the EUC. The means are calculated over all data within 60 km of the desired longitude, so that roughly
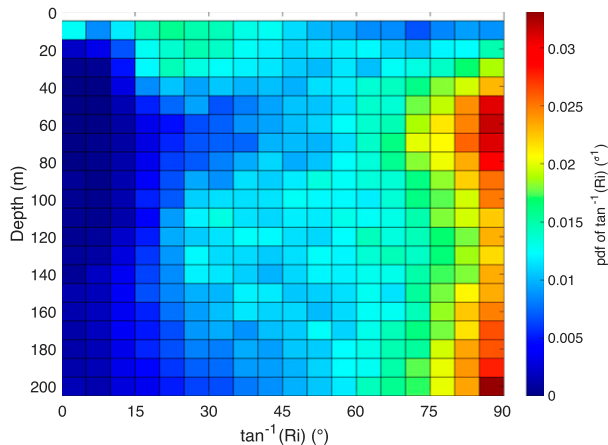
FIG. 16. The probability density function (pdf) of the inverse tangent of the Richardson number, calculated at depth intervals of 10 m, in the upper 200 m. The pdf is calculated in bins of 5° width between 0° and 90°, and is normalized so that the integral of the pdf is equal to one.

2 years of data over a span of 3 years contributed to the calculation. That these features survived the calculation of the mean is a testament to their persistence. With a peak eastward velocity of about $0.5\,\mathrm{m\,s^{-1}}$ in the mean even with a strong El Niño occurring, these glider observations of the EUC corroborate earlier findings that global, coupled general circulation models associated with phase 3 of the Coupled Model Intercomparison Project (CMIP3) severely underestimate the mean EUC at 93°W (peak value $0.2\,\mathrm{m\,s^{-1}}$) (Karnauskas et al. 2012). A more recent analysis of models through CMIP6 also finds model biases in eastward velocity, shear, and stratification (Karnauskas et al. 2020). The relevance of the aforementioned sharp gradients is examined through their effect on potential vorticity Q and Richardson number Ri. The term in the expression for Q involving the vertical shear of eastward velocity is large enough to make the sign of Q opposite to that of the planetary vorticity, especially on the upper southern flank of the EUC. Ri is remarkably low in the mean, underscoring the importance of mixing in the ECS, even at low frequency.

Variability during the 3-yr period October 2013–October 2016 is dominated by the 2014–16 El Niño. Literature on this event is growing (Gasparin and Roemmich 2016; Levine and McPhaden 2016; Chen et al. 2017; L'Heureux et al. 2017; Santoso et al. 2017, 2019; Schönau et al. 2019), and our contribution is notable mainly because of its fine meridional resolution in a strongly affected region—one that is also critical to large-scale ocean–atmosphere coupling à la Bjerknes (1966). The arrival of a downwelling Kelvin wave is apparent in early 2014, as is the subsequent shoaling of the thermocline. There are a series of eastward pulses in the EUC, although they are not related to the arrival of the depressed thermocline. Thus, there is no obvious relationship between the warming characteristic of an El Niño and the strength the EUC on time scales of a few months (Figs. 14 and 15). A notable feature is a fresh anomaly north of the equator during the height of the El Niño

event, possibly related to freshwater flux and advection by a strengthening of the westward SEC.

The concurrent observations of temperature, salinity, and velocity allow discussion of the balances of volume, heat, and salt. Meridional, zonal, and vertical advective terms contribute differently during each ENSO event (Abellán et al. 2018). Persistent divergence throughout the observational period is evident in the mean, and is addressed further using these data in Jakoboski et al. (2020). The heat balance is strongly affected by vertical advection as evidenced by the correlation between temperature and isopycnal displacement (Fig. 14b). This vertical advection is consistent with eastward propagating Kelvin waves seen in Argo data (Fig. 9a). Further, temperature and zonal velocity are uncorrelated suggesting that eastward advection is relatively less important in the heat balance. In contrast, salinity is correlated with eastward velocity, consistent with a source of high salinity in the western Pacific and supporting the importance of eastward advection in the salt balance. There is a similarity between these features of the kinematic balances at the equator and those in eastern boundary regions also affected by El Niño. In particular, the depression of the thermocline, and the arrival of salty water of tropical origin has been noted off California (Lynn and Bograd 2002; Rudnick et al. 2017; Zaba et al. 2020). In the grandest interpretation, El Niños exist in a waveguide stretching across the equatorial Pacific and into the eastern boundaries extending along the coasts of the Americas (Johnson and Obrien 1990). To some degree this interpretation is supported by the arrival of properties downstream along the waveguide, although the leakiness of the waveguide must be acknowledged, especially along the coasts.

An appropriate next step is a quantification of the heat and salt budgets using these data. As has been implemented with sustained glider observations off California, an effective approach is to assimilate the data into an ocean state estimate (Todd et al. 2011, 2012; Zaba et al. 2018, 2020). The ROGER data have already been used in a regional assimilating model (Verdy et al. 2017), and an intention is to pursue an examination of the budgets using a similar approach.

A central result is the presence of low Richardson numbers at the top and bottom of the EUC. The effect of mixing is thus fundamental to quantifying changes of heat and salt. The importance of equatorial mixing is well established, especially by observations from ships and the TAO moorings (Moum et al. 2009, 1992; Perlin and Moum 2012; Lien et al. 1995; Warner and Moum 2019). The deep region of low Ri documented here has been observed previously. For example, Smyth and Moum (2002) show Ri of order one at 180-m depth, 0°N, 140°W from an average of profiles over 5 days. Modeling in Smyth and Moum (2002) suggests that mixing processes at this depth affect the EUC (see also Wang and Muller 2002). The annual cycle of Ri has been calculated using data from the TAO mooring at 0°N, 140°W (Smyth and Moum 2013; Liu et al. 2016; Pham et al. 2017), showing a region of low Ri near the bottom edge of the EUC. In comparison to the ROGER observations at 93°W, the EUC is deeper at 140°W by roughly 20 m (Johnson et al. 2002), so the region of low Ri is deeper at 140°W. The precise values of Ri depend on the methods used to calculate

vertical gradients and to average, with each study using a different method, but the finding of values near one is robust. The ROGER observations are unique in sustaining observations of shear and stratification in a highly resolved section over a period of a few years. The meridional extent of the low Ri region (Fig. 6b) is a new result, to our knowledge. The finding of low Ri from the mean shear and stratification is important, as this mean predisposes the location to even lower shear caused by transient mixing events.

This study was conceived as a sustained 2-yr occupation of 93°W to resolve the equatorial current system west of the Galápagos, and the upwelling and bifurcation of the EUC around the islands. This was motivated in part by a desire to understand the ocean dynamics leading to such a unique, thriving marine and terrestrial ecosystem of the Galápagos (Karnauskas et al. 2015). To be clear, there was no expectation that the measurements would include an El Niño, much less the strongest such event since 1997–98. Given operational challenges, the goal of 2 years of observations on 93°W was achieved, although spread out over 3 years. We fell short of an intention of resolving tropical instability waves (TIWs), which would have required a section every 10 days for a sufficiently high Nyquist frequency. TIWs are certainly part of the variability shown in Figs. 10–13, but the El Niño signal dominates, and the 60-day time scale in our map serves to reduce the effects of TIWs.

Given the diversity of El Niños (Capotondi et al. 2015) it is difficult to say how representative our observations may be of typical conditions. The 110°W section is the nearest on which Johnson et al. (2002) report results distinguished by El Niño and La Niña conditions, where currents during El Niño are found to be weaker. The eastward transports reported here (across 2°S–1°N in the upper 300 m) range from −0.5 to 20.0 Sv with a mean of 8.3 Sv (Fig. 14) during a period mostly considered to be an El Niño as measured by the ONI. This range of transports greatly exceeds the difference between El Niño and La Niña conditions reported in Johnson et al. A detailed comparison between our observations and those of Johnson et al. is probably not warranted. For example, Johnson et al. had a total of 12 sections on 110°W between the years 1991 and 2001. ROGER gliders crossed the equator over 50 times along 93°W during a period of 3 years spanning 2013–16. Perhaps the best way to summarize ROGER results is to say that they emphasize the diversity of conditions during a single El Niño.

5. Conclusions

In conclusion, we have presented highly resolved means and variability of temperature, salinity, and velocity along a section across the equator during the 2014–16 El Niño. To our knowledge, this study comprises the most extensive underwater glider observations ever collected at the equator, much less during a strong El Niño event. Work continues on this dataset, with further possibilities including a study on potential vorticity, analysis of the heat and salt budgets using numerical assimilating state estimates, and an examination of geostrophy close to the equator. The mean potential vorticity and Richardson number suggest the importance of baroclinic,

symmetric, and vertical shear instabilities. A focused study on these instabilities may be worthwhile. The use of autonomous profilers, like gliders or floats, equipped with microstructure sensors in the equatorial region could be an important step forward. To refer back to the essential work of Johnson et al. (2002), we consider the possibility that meridional glider lines could be sustained across the equatorial Pacific. Much of the economy of gliders comes from using small boats launched from land to service the lines, so all the lines considered by Johnson et al. (2002) could not realistically be sustained. However, many lines could reasonably be occupied near land, like these off the Galápagos, and in the low latitude boundary currents of the western Pacific (Davis et al. 2012; Schönau and Rudnick 2017). A future with more autonomous observation in tropical regions is a real possibility.

Data availability statement. Spray glider data are available at spraydata.ucsd.edu (Rudnick et al. 2020). Argo data are available at www.seanoe.org/data/00311/42182/ (Argo 2020). The Roemmich–Gilson Argo climatology was downloaded from sio-argo.ucsd.edu/RG_Climatology.html. The NCEP/NCAR reanalysis 10-m wind was downloaded from www.esrl.noaa.gov/psd/.

REFERENCES

Abellán, E., S. McGregor, M. H. England, and A. Santoso, 2018: Distinctive role of ocean advection anomalies in the development of the extreme 2015–16 El Niño. *Climate Dyn.*, **51**, 2191–2208, https://doi.org/10.1007/s00382-017-4007-0.

Argo, 2020: Argo float data and metadata from Global Data Assembly Centre (Argo GDAC). SEANOE, accessed 24 July 2018, https://doi.org/10.17882/42182.

Bjerknes, J., 1966: A possible response of atmospheric Hadley circulation to equatorial anomalies of ocean temperature. *Tellus*, **18**, 820–829, https://doi.org/10.1111/j.2153-3490.1966.tb00303.x.

Capotondi, A., M. A. Alexander, C. Deser, and M. J. McPhaden, 2005: Anatomy and decadal evolution of the Pacific subtropical-tropical cells (STCs). *J. Climate*, **18**, 3739–3758, https://doi.org/10.1175/JCLI3496.1.

——, and Coauthors, 2015: Understanding ENSO diversity. *Bull. Amer. Meteor. Soc.*, **96**, 921–938, https://doi.org/10.1175/BAMS-D-13-00117.1.

Chen, L., T. Li, B. Wang, and L. Wang, 2017: Formation mechanism for 2015/16 super El Niño. *Sci. Rep.*, **7**, 2975, https://doi.org/10.1038/S41598-017-02926-3.

Davis, R. E., W. S. Kessler, and J. T. Sherman, 2012: Gliders measure western boundary current transport from the South

Pacific to the equator. *J. Phys. Oceanogr.*, **42**, 2001–2013, https://doi.org/10.1175/JPO-D-12-022.1.

Eden, C., and A. Timmermann, 2004: The influence of the Galapagos Islands on tropical temperatures, currents and the generation of tropical instability waves. *Geophys. Res. Lett.*, **31**, L15308, https://doi.org/10.1029/2004GL020060.

Garrett, C., and W. Munk, 1972: Space-time scales of internal waves. *Geophys. Fluid Dyn.*, **3**, 225–264, https://doi.org/10.1080/03091927208236082.

Gasparin, F., and D. Roemmich, 2016: The strong freshwater anomaly during the onset of the 2015/2016 El Niño. *Geophys. Res. Lett.*, **43**, 6452–6460, https://doi.org/10.1002/2016GL069542.

——, and ——, 2017: The seasonal march of the equatorial Pacific upper-ocean and its El Niño variability. *Prog. Oceanogr.*, **156**, 1–16, https://doi.org/10.1016/j.pocean.2017.05.010.

Gill, A. E., 1982: *Atmosphere–Ocean Dynamics*. Academic Press, 662 pp.

Hoskins, B. J., 1974: The role of potential vorticity in symmetric stability and instability. *Quart. J. Roy. Meteor. Soc.*, **100**, 480–482, https://doi.org/10.1002/qj.49710042520.

Hu, S. N., and A. V. Fedorov, 2017: The extreme El Niño of 2015–2016 and the end of global warming hiatus. *Geophys. Res. Lett.*, **44**, 3816–3824, https://doi.org/10.1002/2017GL072908.

Jakoboski, J., R. E. Todd, W. B. Owens, K. B. Karnauskas, and D. L. Rudnick, 2020: Bifurcation and upwelling of the equatorial undercurrent west of the Galapagos archipelago. *J. Phys. Oceanogr.*, **50**, 887–905, https://doi.org/10.1175/JPO-D-19-0110.1.

Jochum, M., and R. Murtugudde, 2006: Temperature advection by tropical instability waves. *J. Phys. Oceanogr.*, **36**, 592–605, https://doi.org/10.1175/JPO2870.1.

Johnson, G. C., and M. J. McPhaden, 1999: Interior pycnocline flow from the subtropical to the equatorial Pacific Ocean. *J. Phys. Oceanogr.*, **29**, 3073–3089, https://doi.org/10.1175/1520-0485(1999)029<3073:IPFFTS>2.0.CO;2.

——, B. M. Sloyan, W. S. Kessler, and K. E. McTaggart, 2002: Direct measurements of upper ocean currents and water properties across the tropical Pacific during the 1990s. *Prog. Oceanogr.*, **52**, 31–61, https://doi.org/10.1016/S0079-6611(02)00021-6.

Johnson, M. A., and J. J. Obrien, 1990: The northeast Pacific Ocean response to the 1982–1983 El Niño. *J. Geophys. Res.*, **95**, 7155–7166, https://doi.org/10.1029/JC095iC05p07155.

Kalnay, E., and Coauthors, 1996: The NCEP/NCAR 40-Year Reanalysis Project. *Bull. Amer. Meteor. Soc.*, **77**, 437–471, https://doi.org/10.1175/1520-0477(1996)077<0437:TNYRP>2.0.CO;2.

Karnauskas, K. B., R. Murtugudde, and A. J. Busalacchi, 2007: The effect of the Galapagos Islands on the equatorial Pacific cold tongue. *J. Phys. Oceanogr.*, **37**, 1266–1281, https://doi.org/10.1175/JPO3048.1.

——, ——, and ——, 2010: Observing the Galapagos–EUC interaction: Insights and challenges. *J. Phys. Oceanogr.*, **40**, 2768–2777, https://doi.org/10.1175/2010JPO4461.1.

——, G. C. Johnson, and R. Murtugudde, 2012: An equatorial ocean bottleneck in global climate models. *J. Climate*, **25**, 343–349, https://doi.org/10.1175/JCLI-D-11-00059.1.

——, S. Jenouvrier, C. W. Brown, and R. Murtugudde, 2015: Strong sea surface cooling in the eastern equatorial Pacific and implications for Galapagos penguin conservation. *Geophys. Res. Lett.*, **42**, 6432–6437, https://doi.org/10.1002/2015GL064456.

——, J. Jakoboski, T. M. S. Johnston, W. B. Owens, D. L. Rudnick, and R. E. Todd, 2020: The Pacific equatorial undercurrent in three generations of global climate models and glider observations. *J. Geophys. Res. Oceans*, **125**, e2020JC016609, https://doi.org/10.1029/2020JC016609.

Lagerloef, G. S. E., G. T. Mitchum, R. B. Lukas, and P. P. Niiler, 1999: Tropical Pacific near-surface currents estimated from altimeter, wind, and drifter data. *J. Geophys. Res.*, **104**, 23 313–23 326, https://doi.org/10.1029/1999JC900197.

Legeckis, R., 1977: Long waves in the eastern equatorial Pacific Ocean: A view from a geostationary satellite. *Science*, **197**, 1179–1181, https://doi.org/10.1126/science.197.4309.1179.

Levine, A. F. Z., and M. J. McPhaden, 2016: How the July 2014 easterly wind burst gave the 2015–2016 El Niño a head start. *Geophys. Res. Lett.*, **43**, 6503–6510, https://doi.org/10.1002/2016GL069204.

L'Heureux, M. L., and Coauthors, 2017: Observing and predicting the 2015/16 El Niño. *Bull. Amer. Meteor. Soc.*, **98**, 1363–1382, https://doi.org/10.1175/BAMS-D-16-0009.1.

Lien, R. C., D. R. Caldwell, M. C. Gregg, and J. N. Moum, 1995: Turbulence variability at the equator in the central Pacific at the beginning of the 1991–1993 El Niño. *J. Geophys. Res.*, **100**, 6881–6898, https://doi.org/10.1029/94JC03312.

Liu, C. Y., A. Kohl, Z. Y. Liu, F. Wang, and D. Stammer, 2016: Deep-reaching thermocline mixing in the equatorial pacific cold tongue. *Nat. Commun.*, **7**, 11576, https://doi.org/10.1038/NCOMMS11576.

Lukas, R., 1986: The termination of the equatorial undercurrent in the eastern Pacific. *Prog. Oceanogr.*, **16**, 63–90, https://doi.org/10.1016/0079-6611(86)90007-8.

——, and E. Firing, 1984: The geostrophic balance of the Pacific equatorial undercurrent. *Deep-Sea Res.*, **31A**, 61–66, https://doi.org/10.1016/0198-0149(84)90072-4.

Lynn, R. J., and S. J. Bograd, 2002: Dynamic evolution of the 1997–1999 El Niño–La Niña cycle in the southern California Current System. *Prog. Oceanogr.*, **54**, 59–75, https://doi.org/10.1016/S0079-6611(02)00043-5.

McPhaden, M. J., 2015: Playing hide and seek with El Niño. *Nat. Climate Change*, **5**, 791–795, https://doi.org/10.1038/nclimate2775.

——, A. J. Busalacchi, and D. L. T. Anderson, 2010: A TOGA retrospective. *Oceanography*, **23**, 86–103, https://doi.org/10.5670/oceanog.2010.26.

Moum, J. N., D. Hebert, C. A. Paulson, and D. R. Caldwell, 1992: Turbulence and internal waves at the equator. Part I: Statistics from towed thermistors and a microstructure profiler. *J. Phys. Oceanogr.*, **22**, 1330–1345, https://doi.org/10.1175/1520-0485(1992)022<1330:TAIWAT>2.0.CO;2.

——, R. C. Lien, A. Perlin, J. D. Nash, M. C. Gregg, and P. J. Wiles, 2009: Sea surface cooling at the equator by subsurface mixing in tropical instability waves. *Nat. Geosci.*, **2**, 761–765, https://doi.org/10.1038/ngeo657.

Perlin, A., and J. N. Moum, 2012: Comparison of thermal variance dissipation rates from moored and profiling instruments at the equator. *J. Atmos. Oceanic Technol.*, **29**, 1347–1362, https://doi.org/10.1175/JTECH-D-12-00019.1.

Pham, H. T., W. D. Smyth, S. Sarkar, and J. N. Moum, 2017: Seasonality of deep cycle turbulence in the eastern equatorial Pacific. *J. Phys. Oceanogr.*, **47**, 2189–2209, https://doi.org/10.1175/JPO-D-17-0008.1.

Riser, S. C., and Coauthors, 2016: Fifteen years of ocean observations with the global Argo array. *Nat. Climate Change*, **6**, 145–153, https://doi.org/10.1038/nclimate2872.

Roemmich, D., and J. Gilson, 2009: The 2004–2008 mean and annual cycle of temperature, salinity, and steric height in the global ocean from the Argo program. *Prog. Oceanogr.*, **82**, 81–100, https://doi.org/10.1016/j.pocean.2009.03.004.

Roundy, P. E., and G. N. Kiladis, 2006: Observed relationships between oceanic Kelvin waves and atmospheric forcing. *J. Climate*, **19**, 5253–5272, https://doi.org/10.1175/JCLI3893.1.

Rudnick, D. L., 2016: Ocean research enabled by underwater gliders. *Annu. Rev. Mar. Sci.*, **8**, 519–541, https://doi.org/10.1146/annurev-marine-122414-033913.

——, and S. T. Cole, 2011: On sampling the ocean using underwater gliders. *J. Geophys. Res.*, **116**, C08010, https://doi.org/10.1029/2010JC006849.

——, R. E. Davis, C. C. Eriksen, D. M. Fratantoni, and M. J. Perry, 2004: Underwater gliders for ocean research. *Mar. Technol. Soc. J.*, **38**, 73–84, https://doi.org/10.4031/002533204787522703.

——, K. D. Zaba, R. E. Todd, and R. E. Davis, 2017: A climatology of the California Current System from a network of underwater gliders. *Prog. Oceanogr.*, **154**, 64–106, https://doi.org/10.1016/j.pocean.2017.03.002.

——, J. T. Sherman, and A. P. Wu, 2018: Depth-average velocity from Spray underwater gliders. *J. Atmos. Oceanic Technol.*, **35**, 1665–1673, https://doi.org/10.1175/JTECH-D-17-0200.1.

——, W. B. Owens, K. B. Karnauskas, and T. M. S. Johnston, 2020: Repeat observations by gliders in the equatorial region. Scripps Institution of Oceanography, Instrument Development Group, accessed 23 March 2020, https://doi.org/10.21238/S8SPRAY0090.

Santoso, A., M. J. Mcphaden, and W. J. Cai, 2017: The defining characteristics of ENSO extremes and the strong 2015/2016 El Niño. *Rev. Geophys.*, **55**, 1079–1129, https://doi.org/10.1002/2017RG000560.

——, and Coauthors, 2019: Dynamics and predictability of El Niño–Southern Oscillation: An Australian perspective on progress and challenges. *Bull. Amer. Meteor. Soc.*, **100**, 403–420, https://doi.org/10.1175/BAMS-D-18-0057.1.

Schönau, M. C., and D. L. Rudnick, 2017: Mindanao Current and Undercurrent: Thermohaline structure and transport from repeat glider observations. *J. Phys. Oceanogr.*, **47**, 2055–2075, https://doi.org/10.1175/JPO-D-16-0274.1.

——, and Coauthors, 2019: The end of an El Niño: A view from Palau. *Oceanography*, **32**, 32–45, https://doi.org/10.5670/oceanog.2019.409.

Sherman, J., R. E. Davis, W. B. Owens, and J. Valdes, 2001: The autonomous underwater glider "Spray." *IEEE J. Oceanic Eng.*, **26**, 437–446, https://doi.org/10.1109/48.972076.

Smith, N., and Coauthors, 2019: Tropical Pacific observing system. *Front. Mar. Sci.*, **6**, 31, https://doi.org/10.3389/fmars.2019.00031.

Smyth, W. D., and J. N. Moum, 2002: Shear instability and gravity wave saturation in an asymmetrically stratified jet. *Dyn. Atmos. Oceans*, **35**, 265–294, https://doi.org/10.1016/S0377-0265(02)00013-1.

——, and ——, 2013: Marginal instability and deep cycle turbulence in the eastern equatorial Pacific Ocean. *Geophys. Res. Lett.*, **40**, 6181–6185, https://doi.org/10.1002/2013GL058403.

Todd, R. E., D. L. Rudnick, M. R. Mazloff, R. E. Davis, and B. D. Cornuelle, 2011: Poleward flows in the southern California Current System: Glider observations and numerical simulation. *J. Geophys. Res.*, **116**, C02026, https://doi.org/10.1029/2010JC006536.

——, ——, ——, B. D. Cornuelle, and R. E. Davis, 2012: Thermohaline structure in the California Current System: Observations and modeling of spice variance. *J. Geophys. Res.*, **117**, C02008, https://doi.org/10.1029/2011JC007589.

——, ——, J. T. Sherman, W. B. Owens, and L. George, 2017: Absolute velocity estimates from autonomous underwater gliders equipped with Doppler current profilers. *J. Atmos. Oceanic Technol.*, **34**, 309–333, https://doi.org/10.1175/JTECH-D-16-0156.1.

Verdy, A., B. D. Cornuelle, M. R. Mazloff, and D. L. Rudnick, 2017: Estimation of the tropical Pacific Ocean state 2010–2013. *J. Atmos. Oceanic Technol.*, **34**, 1501–1517, https://doi.org/10.1175/JTECH-D-16-0223.1.

Wang, D. L., and P. Muller, 2002: Effects of equatorial undercurrent shear on upper-ocean mixing and internal waves. *J. Phys. Oceanogr.*, **32**, 1041–1057, https://doi.org/10.1175/1520-0485(2002)032<1041:EOEUSO>2.0.CO;2.

Warner, S. J., and J. N. Moum, 2019: Feedback of mixing to ENSO phase change. *Geophys. Res. Lett.*, **46**, 13 920–13 927, https://doi.org/10.1029/2019GL085415.

Wyrtki, K., 1975: El Niño—The dynamic-response of equatorial Pacific Ocean to atmospheric forcing. *J. Phys. Oceanogr.*, **5**, 572–584, https://doi.org/10.1175/1520-0485(1975)005<0572:ENTDRO>2.0.CO;2.

Zaba, K. D., D. L. Rudnick, B. D. Cornuelle, G. Gopalakrishnan, and M. R. Mazloff, 2018: Annual and interannual variability in the California Current System: Comparison of an assimilating state estimate with a network of underwater gliders. *J. Phys. Oceanogr.*, **48**, 2965–2988, https://doi.org/10.1175/JPO-D-18-0037.1.

——, ——, ——, ——, and ——, 2020: Volume and heat budgets in the coastal California Current System: Means, annual cycles and interannual anomalies of 2014–16. *J. Phys. Oceanogr.*, **50**, 1435–1453, https://doi.org/10.1175/JPO-D-19-0271.1.

Zaron, E. D., and J. N. Moum, 2009: A new look at Richardson number mixing schemes for equatorial ocean modeling. *J. Phys. Oceanogr.*, **39**, 2652–2664, https://doi.org/10.1175/2009JPO4133.1.